The Effects of Highly Exothermic Chemical Reaction on a Two-Dimensional Mixing Layer

Jay O. Keller*
University of California, Santa Barbara, California
and
J.W. Daily†
University of California at Berkeley, Berkeley, California

An experimental study of the effect of a highly exothermic chemical reaction on a two-stream mixing layer was performed. One stream was lean premixed cold reactants, while the other stream was hot combustion products that acted as an ignition source for the reactants. Results were obtained for a cold to hot side velocity ratio of 15:5 m/s and cold side equivalence ratios ranging from 0 to 0.8. The effect of increasing the energy release was to cause an increase in the acceleration of fluid on the hot, low-velocity side and, thus, an increase in the growth rate of the layer, movement of the centerline position toward the low-velocity side, earlier interaction of the layer with the wall, and a more rapid decay of the Reynolds stresses from their peak values. The large vortex structures that dominated this flowfield were not qualitatively affected by the exothermic reaction. The layer continued to grow by subharmonic combination until wall effects became important. For equivalence ratios less than the lean flammability limit, chemical reaction was restricted to the region of fluid-dynamic mixing. For equivalence ratios greater than the lean flammability limit, however, the reaction zone extended into the irrotational portion of the reactant stream.

Introduction

THE effects of a highly exothermic reaction on a flow in which hot combustion products ignite cold premixed reactants in a two-dimensional free mixing layer have been examined by the authors. The work was motivated by an interest in the characteristics of premixed flames which are stabilized by the recirculation of hot combustion products. The rates at which reactants are consumed, energy released, and pollutant species formed are all influenced by the fluid dynamics of the mixing layer, which, in turn, can be modified by the combustion process.

There has been extensive research on the nature of mixing-layer flows.[1-18] It has been shown that even in the presence of combustion, large vortical structures with an ordered pattern dominate the flowfield.[9] The structures form following the trailing edge of the flow separation element and grow by coalescence and entrainment of fluid from both sides of the layer.[16] Fine-scale mixing occurs within large eddies due to diffusion and small-scale instabilities.[12] In premixed combustors cold reactants and hot products are folded together by entrainment, and combustion occurs when the two fluids are mixed within the eddies.

Measurements of the mean streamwise and transverse velocity components and the Reynolds stresses under circumstances in which the combustor is operated far from acoustic or convective resonances are presented. The data are reduced to show the effects of combustion on the mixing-layer growth rate, centerline position, and peak Reynolds stress. Velocity power spectra and flow-visualization records are presented as well. These data are used to examine the role and behavior of the large-scale vortex structure and the behavior of the reaction zone as a function of equivalence ratio.

In the following the experimental apparatus is described. The results of the measurements are then presented, and their significance discussed. Finally, the work is summarized and relevant conclusions are drawn.

Received Aug. 23, 1983; revision received Feb. 11, 1985.

*Assistant Professor, Department of Mechanical Engineering. Currently, Member of Technical Staff, Sandia National Laboratory, Livermore, CA. Member AIAA.

†Associate Professor, Department of Mechanical Engineering. Member AIAA.

Experimental Facility

Combustion Tunnel

The experiments were carried out in the two-dimensional two-stream combustion tunnel illustrated in Fig. 1. Dried and filtered air was supplied to the inlet of each side. Propane was added to the flow by opposed flow injection in the inlet pipes. On each side there was a venturi contraction section that improved mixing followed by a 750-mm premixing section. The premixing section, with a cross section of 173.1×53.4 mm, was filled with a variety of glass spheres, voids, and, for the last 125 mm, 4.32-mm-diameter metal spheres. This filling filtered acoustic modes, reduced freestream turbulence scales, and provided flashback protection.

Each premixing section was terminated by a flameholder/turbulence suppressor which consisted of three stainless-steel screens separated by 8-mm gaps. A flat, preheat flame could be stabilized on either side of the tunnel to provide hot combustion products as an inlet condition.

The test section followed a 2.7:1 contraction section. The flow was separated in the contraction section by a tapered splitter plate constructed from Space Shuttle insulating tile material. The test section was 122.2 mm wide, 56.9 mm high, and 229 mm long. All four sides of the test section were made of quartz for full optical access.

Following the test section was a diffuser that employed boundary-layer suction to reduce acoustic noise. The combustion products were then introduced into a low-pressure exhaust system through a series of water sprays which cooled the gas. The pressure in the test section was set to 1 atm using a butterfly valve in the exhaust pipe.

Considerable attention was paid to finding operating conditions far from acoustic or convective resonances.[16] In addi-

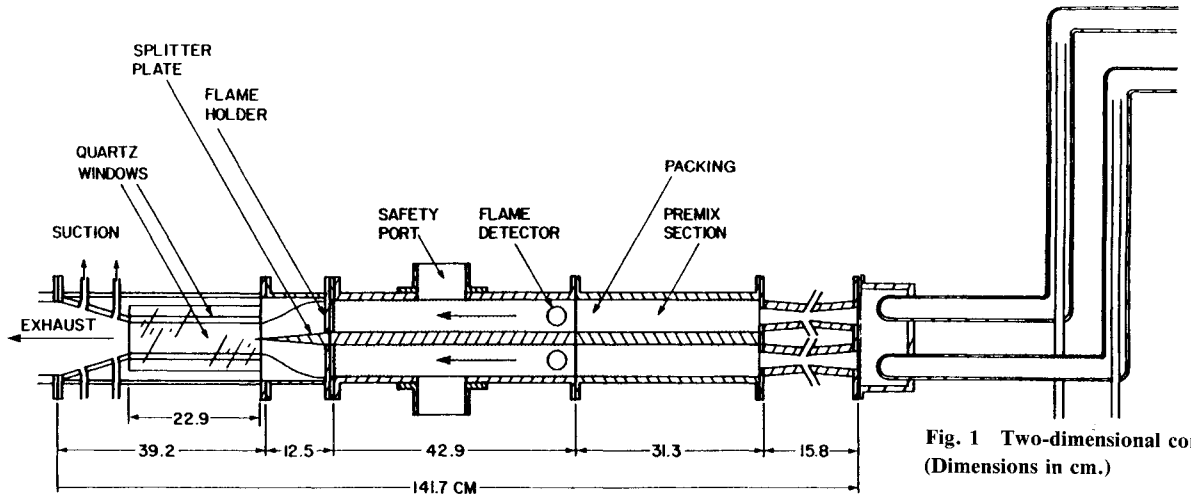

Fig. 1 Two-dimensional combustion facility. (Dimensions in cm.)

tion, numerous measurements were made to ensure that the mean flow was reasonably two-dimensional.

Instrumentation

Laser Anemometer

Velocity was measured using a dual-beam, real-fringe interferometer laser Doppler anemometer (LDA) with a probe volume whose largest dimension was 131 μm. The Doppler frequencies were analyzed by a period counter which allowed the time between realizations to be recorded.

Joint records of the streamwise and transverse velocity components as a function of time were used to construct velocity probability distribution functions (pdf), the first four moments of velocity, and the Reynolds stresses. The data rates achieved were always higher than 1 kHz.

Velocity power spectra were obtained by analyzing the analog output of the signal processors with a Model 512 General Radio frequency analyzer. For the power spectra calculations, the system was operated such that the data rates were extremely high—greater than 10kHz. The records were averaged until the power spectra were stationary, typically over 1024 spectra.

Cyclone particle seeders similar to those described by Pitz[13] were used to suspend alumina (Al_2O_3) particles in the flow. The alumina particles (0.05 μm nominal diameter) were dried before each experiment to limit their agglomeration. The average particle diameter in the airstream was estimated to be 0.2 μm. This particle size provides a frequency response of 10 kHz for a 1% velocity lag.[19]

The minimum uncertainty possible for a velocity realization is determined by the counter clock resolution and frequency spacing uncertainty. This was 0.4% for the system presented herein. Other errors may arise in LDA measurements because of velocity biasing, uneven seeding in the two sides, interference fringe curvature, Bragg cell imperfections or misalignment, and beam steering due to density variations. Velocity biasing and uneven seeding effects were circumvented by the use of time-integrated averages[20] as mentioned previously. Interference fringe curvature from misplacement of the beam waist added a less than 1% error to the velocity measurements. Bragg cell and density variation effects corrections, as well as other sources of error, are discussed in detail by Pitz.[13] It is estimated that the combined uncertainty due to a variety of effects is about 2%.

Schlieren System

The system was a typical Z configuration using a horizontal rectangular schlieren stop. The system was used for both high-speed cinematography and spark photographs. A Hy-cam camera operating at 5000 frames per second was used for the high-speed cinematography. Flame-illuminated and long time-exposure and spark schlieren photographs were recorded with a 4×5 Polaroid camera.

Pressure Gradient

The streamwise pressure gradient was measured by a Baratron pressure gage.

Experimental Results

Operating Conditions

For this study the velocity ratio across the layer was held constant, as were the inlet temperatures. The equivalence ratio on the cold, high-velocity side of the layer was varied from 0 to 0.8 in steps of 0.2 (see Table 1). The hot, low-velocity side consisted of the products of propane-air combustion with an equivalence ratio of 0.64. For purposes of comparison, the isothermal, room-temperature case is presented as well.

Inlet Conditions

Figure 2 shows entrance profiles for the isothermal case. (The entrance data were taken 2 mm downstream of the splitter plate because of optical access limitations.) The upper plot in Fig. 2 shows the average streamwise velocity U and the turbulence intensity u/Uc vs the transverse location y. The freestream turbulence-intensity level was approximately 1.9% for both the high- and low-velocity sides (sides 1 and 2, respectively).

The lower plots in Fig. 2 show the inlet boundary-layer velocity and turbulent-intensity profiles in more detail. The solid lines are the Blasius profiles for each case. y was normalized by the displacement thickness and the velocities were normalized by the freestream velocity. The Reynolds numbers based on the displacement thickness for sides 1 and 2 were 355 and 230, respectively. The shape factors for the boundary layers on sides 1 and 2 were 2.44 and 2.41, respectively.

Figure 3 shows entrance conditions typical of all of the energy release cases studied. This figure is plotted in the same format as Fig. 2. The shape factors for these layers were 2.40 and 2.51 for sides 1 and 2, respectively. The Reynolds numbers for sides 1 and 2 were 554 and 52, respectively.

Power spectra of the streamwise velocity taken in the freestream are shown in Fig. 4 for the isothermal case and in Fig. 5 for a typical energy release case. The spectra were normalized by area and plotted on the same scale for comparison. (The power spectra for the low-velocity side of Fig. 5 appear to have an area of less than 1. This is caused by a significant contribution to the area by low frequencies which are not well represented in the figure.) As can be seen, there are no major resonances present in the inlet flow and the spectra are characteristic of grid turbulence.

Table 1 Operating conditions

Case No.	Side 1 U, m/s	Side 1 T, K	ϕ	Side 2 U, m/s	Side 2 T, K
1	15	293.0	0.00	5	293.0
2	15	293.0	0.00	5	1770.0
3	15	293.0	0.20	5	1770.0
4	15	293.0	0.40	5	1770.0
5	15	293.0	0.60	5	1770.0
6	15	293.0	0.80	5	1770.0

Note: Operating conditions for the six cases examined in this investigation are given. No LDV mean data were obtained for the 0.8 equivalence ratio case because there was excess heating of the apparatus.

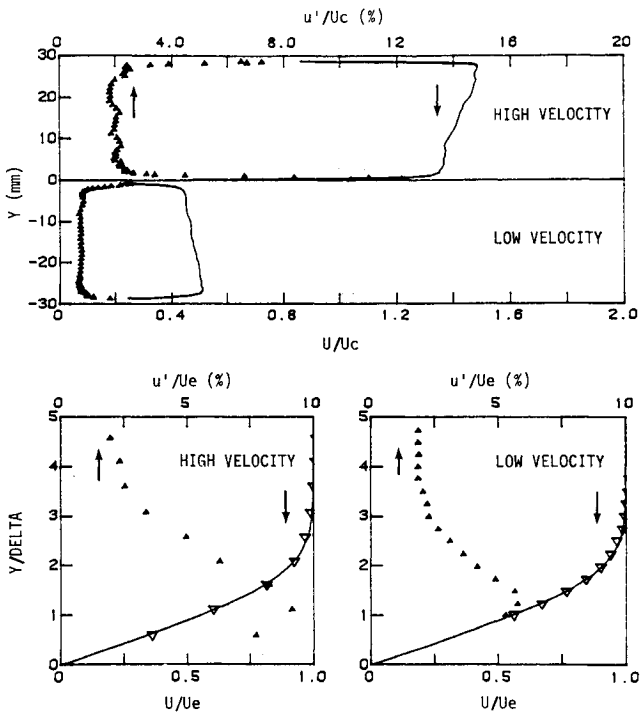

Fig. 2 Isothermal case entrance profiles of the mean streamwise velocity and turbulent intensity. Top: full profiles, bottom: expanded boundary-layer profiles. Solid lines in bottom figures are Blasius profiles.

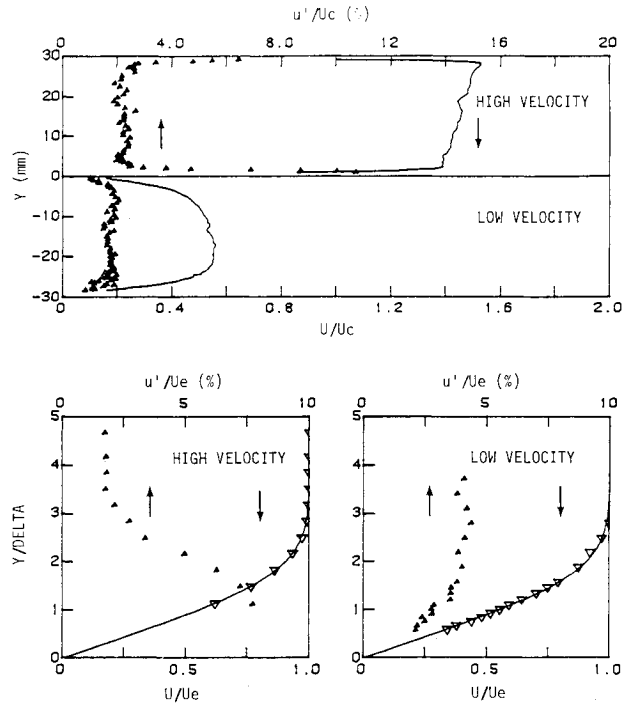

Fig. 3 Nonisothermal case entrance profiles of the mean streamwise velocity and turbulent intensity. Top: full profiles, bottom: expanded boundary-layer profiles. Solid lines in bottom figures are Blasius profiles.

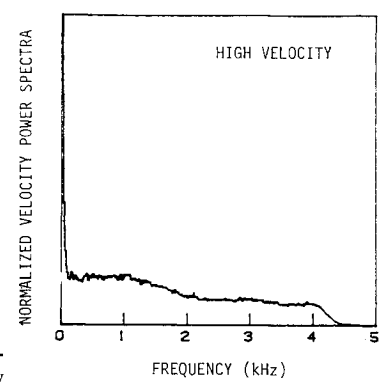

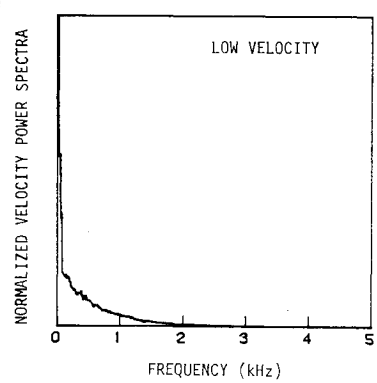

Fig. 4 Normalized entrance streamwise velocity power spectra for the isothermal case.

Velocity Field

Mean velocity components were calculated from velocity records measured at nine streamwise locations for cases 1-5 (Table 1). Figure 6 shows profiles of the streamwise mean velocity U as a function of streamwise position x and equivalence ratio. Figure 7 shows profiles of the transverse mean velocity V. Both are normalized by Uc, the mean mass-averaged convection velocity. The first case plotted in each figure is the isothermal flow.

Reynolds Stresses

Reynolds stresses were also calculated. Figure 8 shows the cross-correlation Reynolds stress profiles as a function of the streamwise position and the equivalence ratio. The peak Reynolds stresses for all of the cases are shown in Fig. 9. Both results are also normalized on Uc.

Other Moments

In addition to the Reynolds stresses, third and fourth moments of velocity were calculated for all of the cases. Of use in this analysis are the streamwise skewness profiles shown in Fig. 10 as a function of streamwise position and equivalence ratio.

Velocity Power Spectra

In addition to the mean data, power spectra were obtained at a number of locations. Figure 11 shows normalized transverse power spectra taken at the point in the mixing layer where the mean streamwise velocity is equal to the mass-averaged convection velocity as a function of streamwise position.

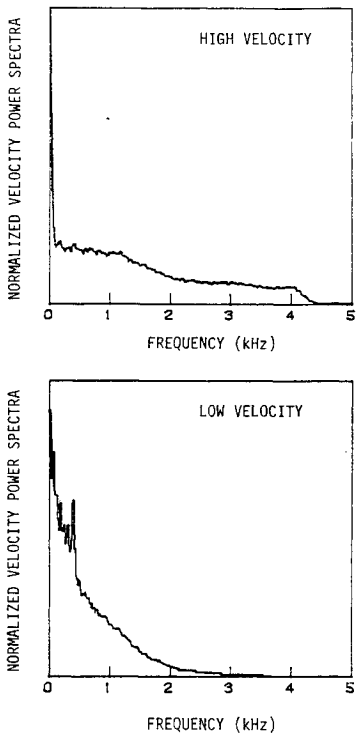

Fig. 5 Normalized entrance streamwise velocity power spectra, which are typical of the energy release cases.

Visualization

Figure 12 shows spark schlieren photographs for cases 2-6. Figure 13 shows a sequence of frames, 1.3 ms apart, from a high-speed schlieren movie of case 2. Flame-illumination, long time-exposure photographs are shown in Fig. 14 for cases 3-6.

Eddy Passing Frequencies

The schlieren movies were analyzed to provide spectral information regarding the formation and passage of large eddy structures. Figure 15 shows the passing frequency for all of the hot cases.

Pressure Gradient

The streamwise pressure gradient was measured for each case and the results are shown in Fig. 16. The pressure gradient was normalized on the dynamic pressure based on the cold inlet density, the convection velocity, and the distance between the pressure ports, 180 mm, which is approximately the length of the combustor.

Discussion

Mean Flow Behavior

The mean data for the isothermal flow are typical of free mixing layers. The mean axial velocity profile has an error-function-type shape. Because the pressure gradient is favorable, the transverse velocity, except at the inlet, is negative. The Reynolds stresses display a behavior that is typical of layers developing from laminar boundary layers.[2]

There are a number of differences between the reacting cases and the isothermal case. The mean streamwise and transverse velocity profiles develop somewhat differently, as do the peak Reynolds stresses. One may see that increasing the heat release rate accelerates the low-velocity, low-density fluid, while the high-velocity fluid changes little. One may explain this behavior by the following arguments.

Since the freestream is approximately unidirectional, the x- and y-momentum equations can be written as

$$\rho U\frac{\mathrm{d}U}{\mathrm{d}x}=-\frac{\mathrm{d}P}{\mathrm{d}x},\qquad \frac{\mathrm{d}P}{\mathrm{d}y}=0 \tag{1}$$

For isothermal flow and equivalence ratios greater than 0.4, the pressure gradient is favorable. (For the other cases the

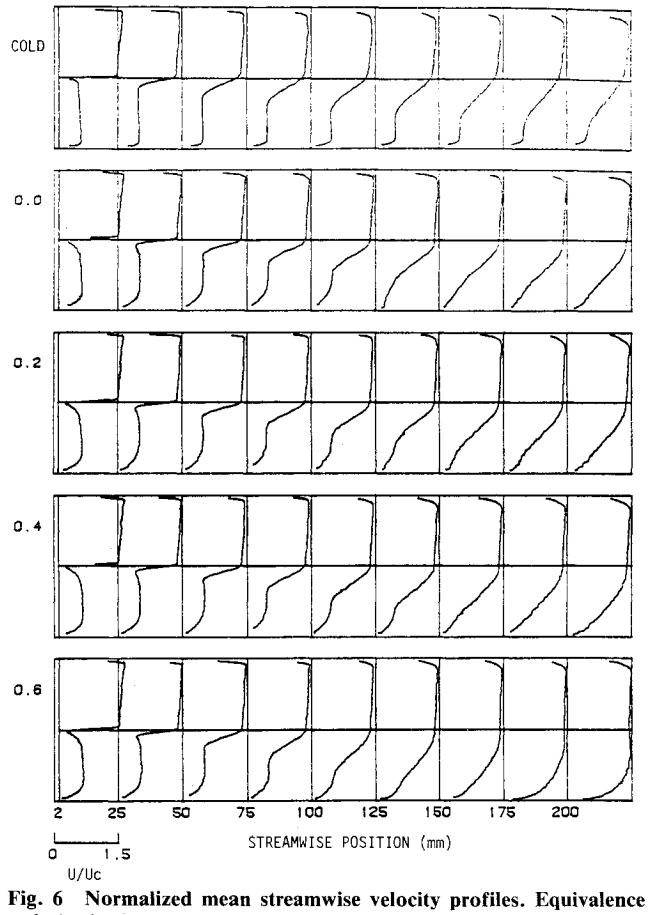

Fig. 6 Normalized mean streamwise velocity profiles. Equivalence ratio is given at the left; streamwise position is at the bottom.

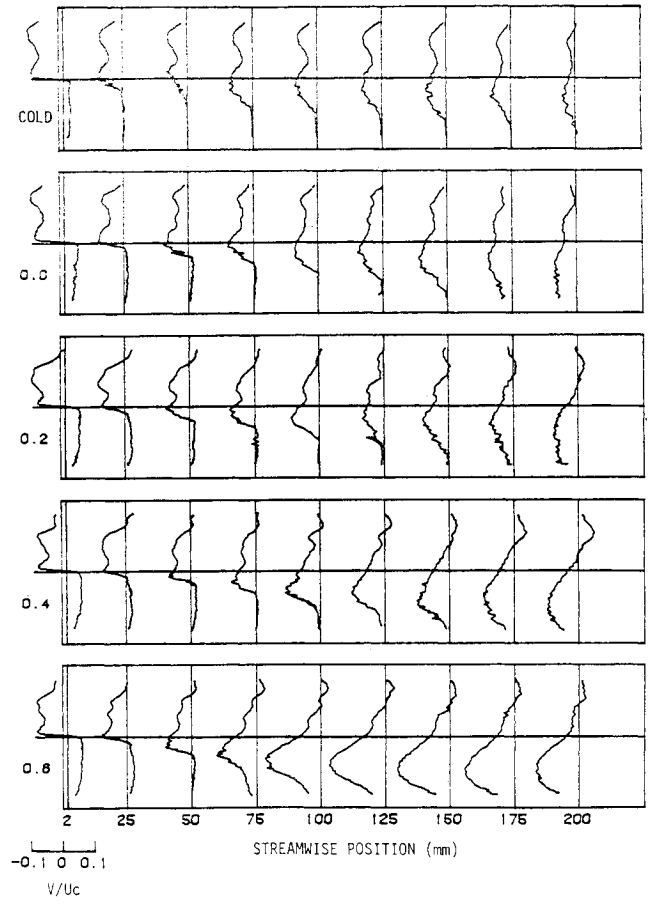

Fig. 7 Normalized mean transverse velocity profiles. Equivalence ratio is given at the left; streamwise position is at the bottom.

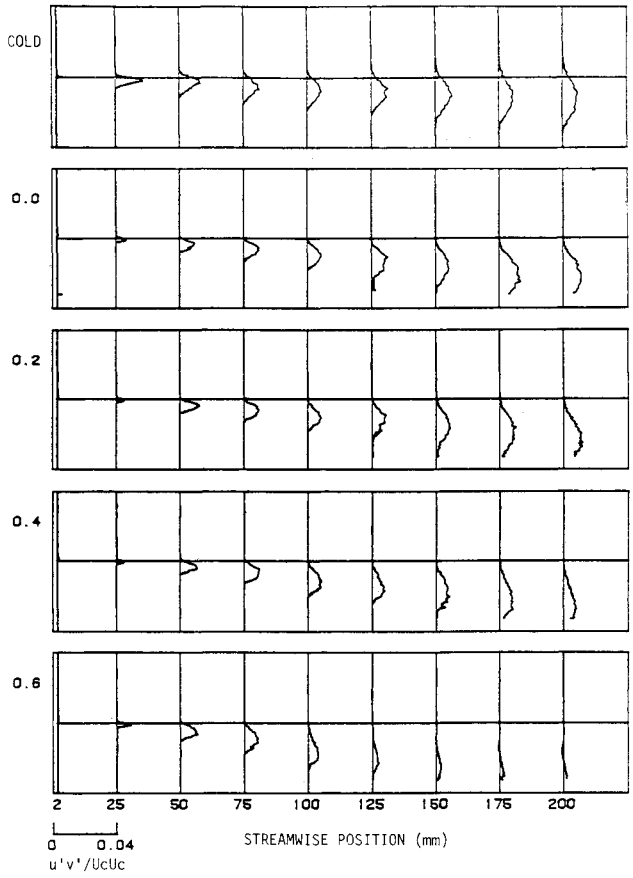

Fig. 8 Normalized Reynolds stress profiles. Equivalence ratio is given at the left; streamwise position is at the bottom.

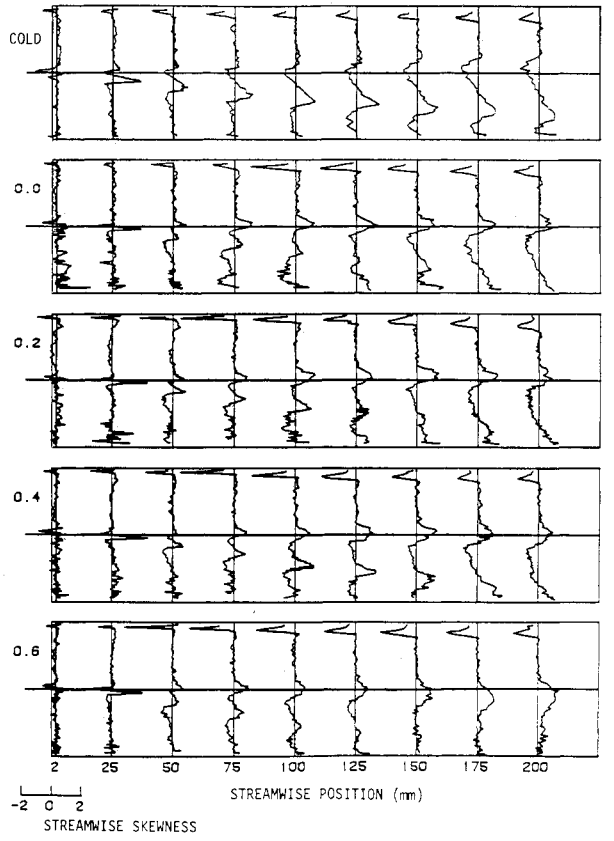

Fig. 10 Streamwise skewness profiles as a function of equivalence ratio and streamwise position. Equivalence ratio is given at the left; streamwise position is at the bottom.

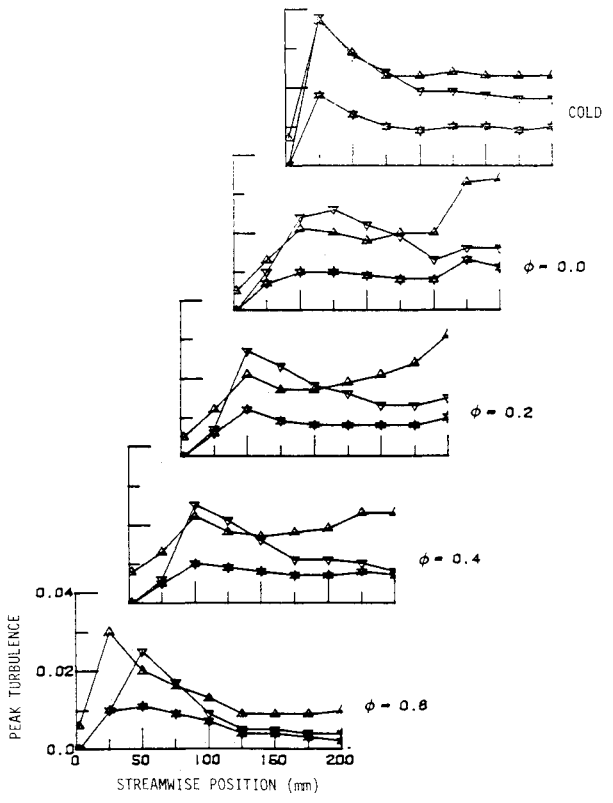

Fig. 9 Normalized peak Reynolds stresses as a function of streamwise position. Δ: $u'u'/UcUc$; ▽: $v'v'/UcUc$; *: $u'v'/UcUc$. Equivalence ratio is given at the right.

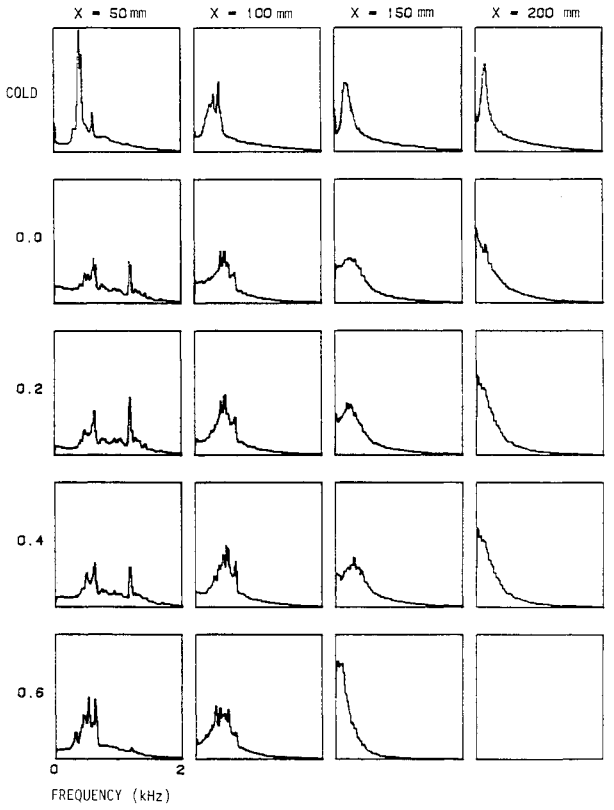

Fig. 11 Normalized transverse power spectra as a function of streamwise position and equivalence ratio. Equivalence ratio is given at the left; streamwise position at the top. The data were taken where the mean streamwise velocity is equal to the mass-averaged convection velocity.

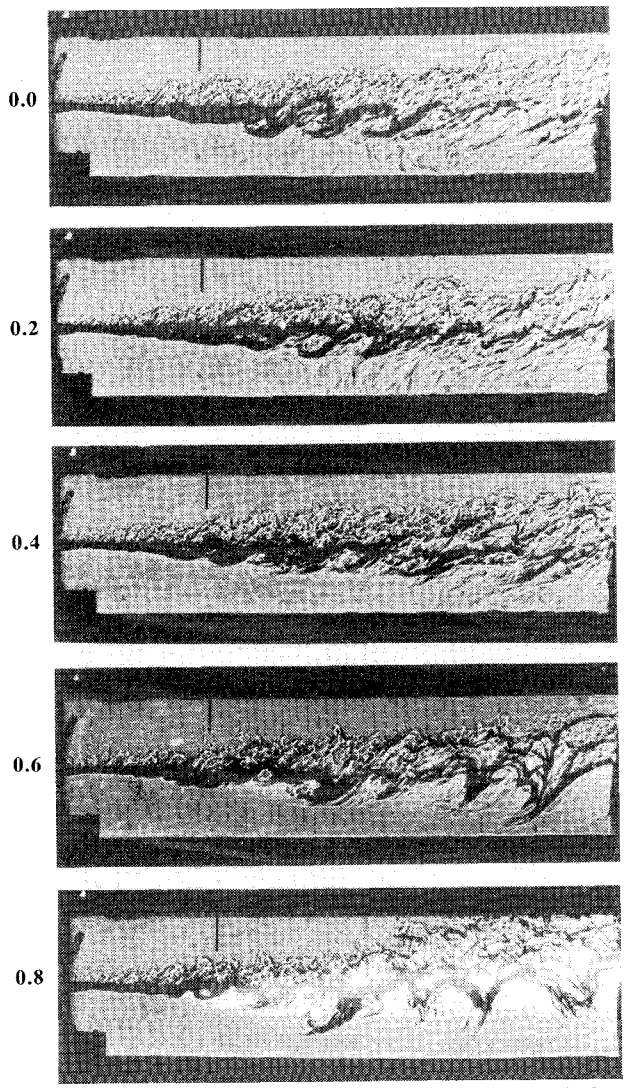

Fig. 12 Spark schlieren photographs for cases 2-6 with equivalence ratios at left.

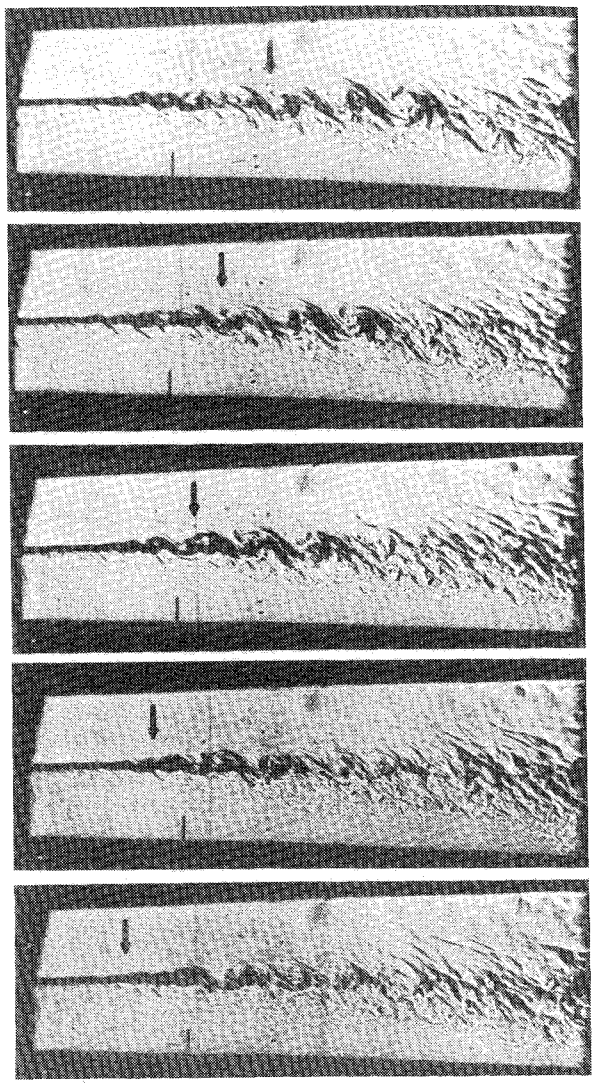

Fig. 13 High-speed schlieren movie sequence for case 2. The individual frames are 1.3 ms apart.

pressure gradient is almost zero.) For a favorable pressure gradient, dU/dx is positive for all y. Applying Eq. (1) to both sides of the layer, we obtain

$$\frac{[dU/dx]_1}{[dU/dx]_2} = \frac{(\rho U)_2}{(\rho U)_1} \tag{2}$$

Since the momentum ratio across the layer is about 1:18, the low-velocity, low-density side will be affected much more by the favorable pressure gradient than the high-velocity, high-density side.

For $\phi = 0.6$ the density within the mixing layer is approximately the same as on the hot side. Assuming, to first order, that the flow may be divided into two constant-density regions with a discontinuity at the upper edge of the mixing layer, we may integrate the continuity equation across each region obtaining

$$v(y) = -\int \frac{\partial U}{\partial x} dy + v(0) \tag{3}$$

Since $\partial U/\partial x$ is positive for this case, v will be negative throughout the flowfield, as is seen in Fig. 7. Note that this argument also applies to the isothermal case for which the density is constant.

Although the pressure gradient is zero for the $\phi = 0.0$, 0.2, and 0.4 cases, continuity requires that the average velocity must increase with increasing heat release since the mass flow rate is constant and the average density is decreasing. Equation (2) is still valid in these cases and, thus, one expects the major increase in velocity to be seen on the low-density side. This is borne out in Fig. 6. Since $\partial U/\partial x$ is positive in these cases as well, the transverse velocity should mostly be negative as is confirmed by examination of Fig. 7.

The data were further reduced by fitting the streamwise velocity profiles to an error function using a least-squares algorithm. (At large streamwise distances and large heat release, some of the profiles did not have an error function shape and so fitting was not attempted.) From the fit, the mixing-layer vorticity (maximum velocity gradient) thickness and centerline position were calculated.[5]

Figure 17 shows the vorticity thickness as a function of streamwise position and equivalence ratio. Figure 18 shows the position of the mixing-layer centerline as a function of the streamwise position and equivalence ratio.

The average slopes of the data in Figs. 17 and 18 are measures of the growth and offset rates, respectively. These slopes are plotted in Fig. 19 as functions of the streamwise position and equivalence ratio. The top figure is the vorticity thickness growth rate ($d\delta_\omega/dx$), and the bottom figure is the mixing-layer offset rate (dY_0/dx). The figures demonstrate a smooth but rapid change in the mixing-layer growth rate and offset rate as the amount of energy release is increased.

These results are consistent with the analysis given above. The growth of the mixing layer is associated with the accelera-

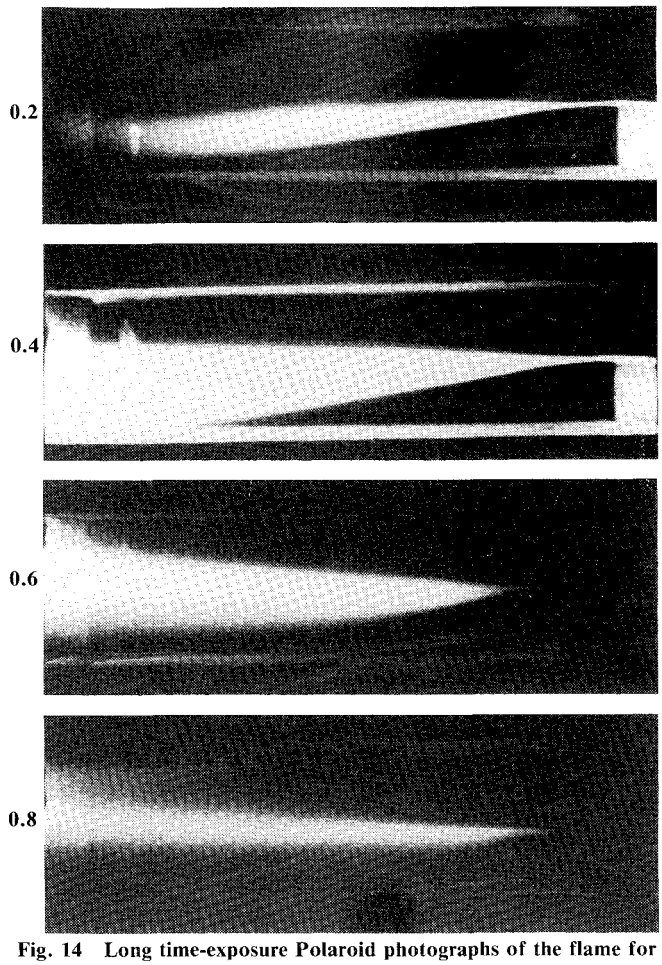

Fig. 14 Long time-exposure Polaroid photographs of the flame for cases 2-6. Equivalence ratio at left.

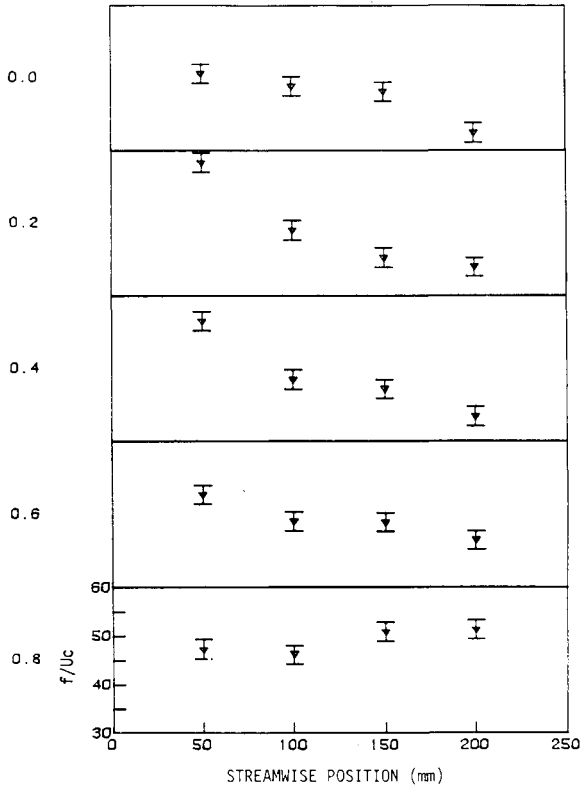

Fig. 15 Eddy passing frequency as a function of streamwise position and equivalence ratio, obtained from schlieren movies. Equivalence ratio is given on the left; streamwise position is at the bottom.

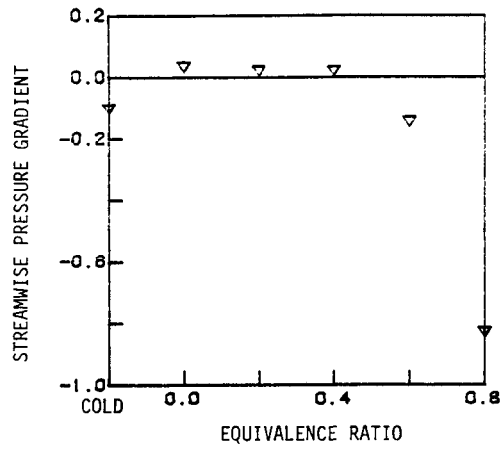

Fig. 16 Normalized average streamwise pressure gradient as a function of equivalence ratio.

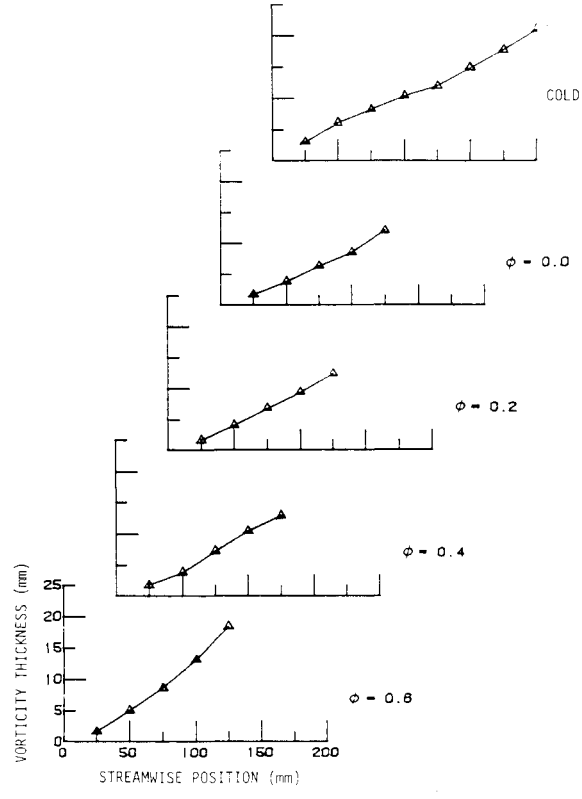

Fig. 17 Vorticity thickness as a function of streamwise position and equivalence ratio. Equivalence ratio is given at the right.

tion of the low-speed, low-density fluid which is enhanced by increasing heat release. Likewise, because the high-velocity, high-density side remains largely unaffected, the effective centerline of the layer will be shifted toward the low-speed, low-density side, causing earlier interaction of the layer with the wall, and this shifting will also be enhanced by increased heat release. The change with equivalence ratio is rapid because the heat release is a nonlinear function of equivalence ratio.

The behavior of the Reynolds stresses is difficult to explain without knowledge of the three-dimensional structure. As discussed in Refs. 17 and 18, the peak is associated with the early, highly correlated portion of the mixing layer, while the decay occurs as a result of loss of coherence.

However, since the initial velocity gradient across the layer and the layer initial conditions are the same for all of the cases studied, one would expect that the initial stresses would be about the same for each case, which they are to first order.

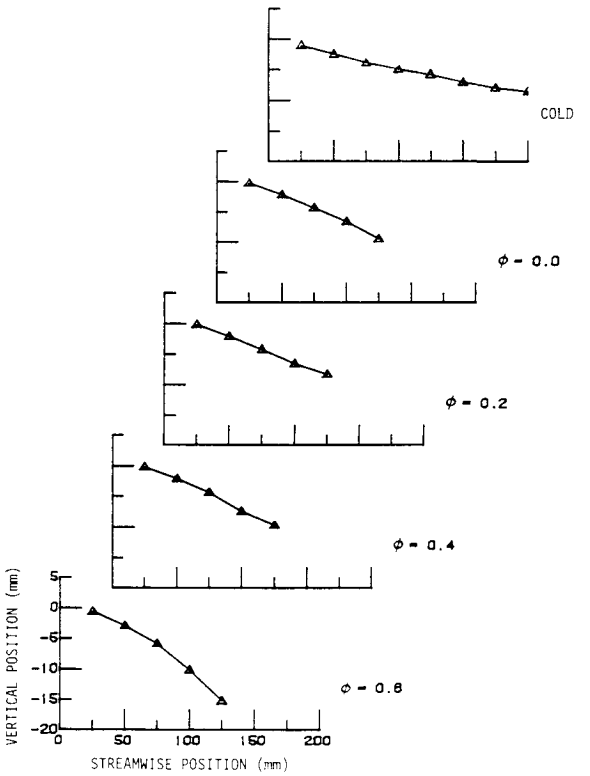

Fig. 18 Mixing layer centerline as a function of streamwise position and equivalence ratio. Equivalence ratio is given at the right.

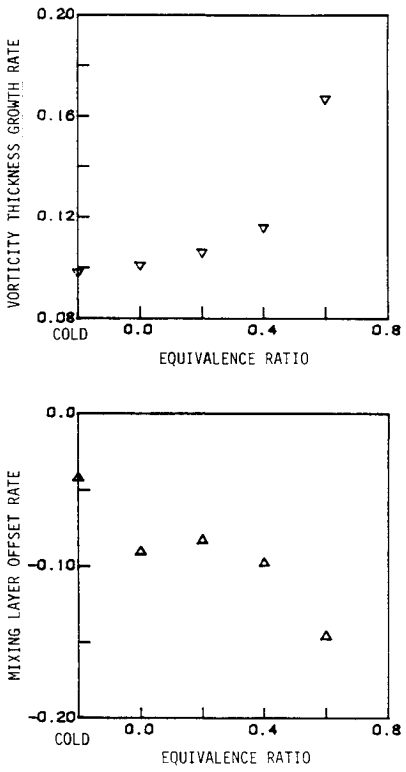

Fig. 19 Mixing-layer growth rate $d\delta\omega/dx$ (top) and offset rate dY_0/dx (bottom) as functions of equivalence ratio.

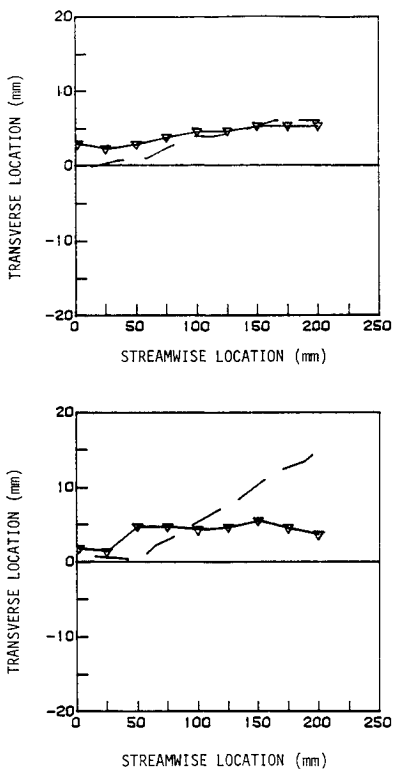

Fig. 20 Comparison between boundary deduced from skewness (triangles) and flame boundary from long time-exposure photographs (dashed line). The first plot is case 4, the second is case 5.

Also, because the layer grows faster as the amount of heat release is increased, the velocity gradient across the layer correspondingly drops faster. Thus one would expect the stresses to decrease from their peak more rapidly at the higher equivalence ratios. This is seen in Fig. 9. The actual values of the stresses, however, depend on the structure of the flow and the degree of coherence.

Large-Scale Vortex Structure

There can be no question about the existence of large-scale, Kelvin-Helmholtz-type, two-dimensional vortex structures in this flow. The schlieren visualization allows one to examine the entire flowfield directly and at all equivalence ratios the structures are visible in the spark photographs (Fig. 12) and movies (Fig. 13). Furthermore, there appears to be no qualitative change in the nature of the mixing layer due to either the imposition of a large temperature difference or heat release. There is no evidence to conclude that the initial breakdown of the layer occurs by any mechanism other than the Kelvin-Helmholtz rollup.

The data show that the growth of the layer continues to occur via subharmonic combination until the walls inhibit further rollup. One may observe subharmonic combination of the structures in schlieren records for all cases up to the point where combination produces structures that significantly interact with the wall. The arrow in the sequence of Fig. 13 follows a pairing of two adjacent vortices. Once pairing ceases, the structures are seen in the movies to be convected downstream at the mean velocity.

These conclusions are borne out by both the velocity power spectra data of Fig. 11 and the passing frequency data of Fig. 15. One may see the decrease in frequency associated with subharmonic combination for equivalence ratios up to and including 0.6—the cases for which the layer did not begin to interact with the wall prior to the last sampling station. For the highest equivalence ratio, however, the layer growth rate was such that the layer began to interact with the walls approximately 100-125 mm from the splitter plate (see Fig. 16). The vortex passing frequency ceases to drop past this point and, in fact, increases a small amount.

Flame Spread

The rate at which the flame spreads into the unburned reactants is important in practical burner design. For a pilot stabilized flow, most, if not all, of the reactants entrained into

the mixing layer will burn regardless of the equivalence ratio. At high enough equivalence ratios, however, the laminar flame speed will differ from zero, allowing the flame to propagate into the premixed reactants.

To study flame spread, flame-illuminated photographs were taken such as those shown in Fig. 14. From these photographs one may obtain an estimate of the outermost limit of flame excursion. From schlieren records and the velocity measurements, one may see that the outer limit of significant rotational behavior, corresponding to the "visual thickness" of Ref. 5, is well identified by the point where the streamwise velocity skewness goes to zero (Fig. 10).

Thus both the flame excursion boundary (from Fig. 12) and the position of zero streamwise velocity skewness against streamwise distance were plotted together. The results are shown in Fig. 20 for cases 4 and 5.

For case 4 the reactants were at an equivalence ratio below the lean flammability limit and, as seen, the visual flame remains entirely within the rotational region. For case 5, however, the laminar flame speed is different from zero and the flame propagates beyond the layer.

The location of the flame front was found to be restricted to the region of fluid-dynamic mixing for equivalence ratios below the lean flammability limit. However, for equivalence ratios greater than the lean flammability limit the reaction zone extended beyond this region.

Summary and Conclusions

A study of a two-stream mixing layer, where one stream was hot combustion products and the other stream was cold unburnt reactants, was performed. Joint streamwise and transverse velocity records were measured and from them the first four moments of velocity and the Reynolds stress terms were calculated. Schlieren photography was used to visualize the flowfield, yielding time-resolved visual information in the form of spark photographs and high-speed movies. Long-time Polaroid photography of the chemical luminescence provided time-averaged visualization of the chemical reaction zone. The channel pressure gradient was also measured.

Results were obtained for a cold to hot side velocity ratio of 15:5 m/s and cold side propane air equivalence ratios ranging from 0.0 to 0.8. The hot side propane/air equivalence ratio was 0.64, providing an inlet temperature of 1770 K. Results were also obtained for the isothermal case.

The major effect of heat release was to cause (by continuity) fluid in the channel to accelerate. Because of the large momentum ratio across the layer, the effect was much larger for the low-density, low-velocity side. Thus, the layer grew faster into the low-density, low-speed side as the amount of heat release was increased. The enhanced growth rate meant that the layer interacted with the wall sooner as the heat release was increased and that the Reynolds stresses decreased more rapidly from their peak values.

The large vortex structures that dominate this flowfield were not qualitatively affected by the exothermic chemical reaction. The layer continued to grow by subharmonic combination until wall effects became important. Once subharmonic combination ceased, the structures were convected downstream as individual fluid elements.

For equivalence ratios less than the lean flammability limit, chemical reaction was restricted to the region of fluid-dynamic mixing. However, for equivalence ratios greater than the lean flammability limit the reaction zone extended into the irrotational portion of the reactant stream.

Acknowledgments

The authors gratefully acknowledge support from National Science Foundation Grant ENG 77-02019 and Contract ARO-5-82 through Alfred Buckingham and Wigbert Siekhaus at Lawrence Livermore National Laboratory.

References

[1]Batt, R.G., "Turbulent Mixing of Passive and Chemically Reacting Species in a Low-Speed Shear Layer," *Journal of Fluid Mechanics*, Vol. 82, 1977, pp. 53-95.

[2]Birch, S.F., "Data Evaluation Report for Free Mixing Layers," Report prepared for the 1980/81 Stanford Conferences on Complex Turbulent Flows, Stanford University, Stanford, CA, 1980.

[3]Bradshaw, P., "The Effect of Initial Conditions on the Development of a Free Shear Layer," *Journal of Fluid Mechanics*, Vol. 26, 1966, pp. 225-236.

[4]Breidenthal, R.E., "A Chemical Reacting Turbulent Shear Layer," Ph.D. Thesis, California Institute of Technology, Pasadena, CA, 1978.

[5]Brown, G. and Roshko, A., "On Density Effects and Large Structures in Turbulent Mixing Layers," *Journal of Fluid Mechanics*, Vol. 64, 1974, p. 775.

[6]Corcos, G.M. and Sherman, F.S., "Vorticity Concentration and the Dynamics of Unstable Force Shear Layers," *Journal of Fluid Mechanics*, Vol. 73, 1976, p. 241.

[7]Dimotakis, P.E. and Brown, G.L., "The Mixing Layer at High Reynolds Number: Large Structure Dynamics and Entrainment," *Journal of Fluid Mechanics*, Vol. 78, 1976, pp. 535-560.

[8]Fiedler, H., Korschelt, D., and Mensing, P., "On Transport Mechanism and Structure of Scalar Field in a Heated Plane Shear Layer," *Lecture Notes in Physics, Symposium on the Structure and Mechanisms of Turbulence II*, Springer-Verlag, Berlin, 1977, pp. 58-72.

[9]Ganji, A.R. and Sawyer, R.F., "An Experimental Study of the Flow Field and Polluted Formation in a Two Dimensional, Premixed, Turbulent Flame," AIAA Paper, Jan. 1979.

[10]Ghoniem, A.F., Chorin, A., and Oppenheim, A.K., "Numerical Modeling of Turbulent Combustion in Premixed Gases," *Eighteenth Symposium (International) on Combustion*, The Combustion Institute, Pittsburgh, PA, 1981 (in press).

[11]Husain, Z.D. and Hussain, A.K.M.F., "Axisymmetric Mixing Layer: Influence of the Initial and Boundary Conditions," *AIAA Journal*, Vol. 17, 1979, pp. 48-55.

[12]Konrad, J.H., "Experimental Investigation of Mixing in Two Dimensional Turbulent Shear Flows with Application to Diffusion-Limited Reactions," SQUID Rept. CIT-8-PU, 1976.

[13]Pitz, R.W., "An Experimental Study of Combustion: The Turbulent Structure of a Reacting Shear Layer Formed at a Rearward-Facing Step," Ph.D. Thesis, University of California, Berkeley, 1981.

[14]Roshko, A. and Bernal, L., "Organized Structure in Turbulent Shear Flow and Development of a Smaller Scale," Paper presented at the First Annual California University Fluid Mechanics Retreat, Stanford University, Stanford, CA, April 1981.

[15]Winant, C.C. and Browand, F.K., "Vortex Pairing: The Mechanism of Turbulent Mixing-Layer Growth at Moderate Reynolds Number," *Journal of Fluid Mechanics*, Vol. 63, 1974, p. 237.

[16]Keller, J.O., Vaneveld, L., Korschelt, D., Ghoniem, A.F., Daily, J.W., and Oppenheim, A.K., "Mechanisms of Instabilities in Turbulent Combustion Leading to Flashback," *AIAA Journal*, Vol. 20, 1982, p. 254.

[17]Bradshaw, P., "The Effect of Initial Conditions on the Development of a Free Shear Layer," *Journal of Fluid Mechanics*, Vol. 26, 1966, p. 225.

[18]Daily, J.W. and Lundquist, W.J., "Three Dimensional Structure in a Turbulent Combusting Mixing Layer," 20th Symposium on Combustion, Ann Arbor, MI, 1984.

[19]Durst, F., Melling, A., and Whitelaw, J.H., *Principles and Practice of Laser-Doppler Anemometry*, Academic Press, New York, 1976.

[20]Dimotakis, P.E., "Single Scattering Particle Laser Doppler Measurements of Turbulence," AGARD 193.